Static strength and fatigue life of pinned hybrid titanium-composite single-lap-shear joints

Kralovec, Christoph; Dengg, Andreas; Schagerl, Martin; Schiller, Arne; Bisagni, Chiara; Loebbecke, Miriam; Haubrich, Jan; Hanelt, Robert

Important note
To cite this publication, please use the final published version (if applicable).
Please check the document version above.

Static strength and fatigue life of pinned hybrid titanium-composite single-lap-shear joints

Christoph Kralovec [a],*, Andreas Dengg [a], Martin Schagerl [a], Arne Schiller [b], Chiara Bisagni [c], Miriam Loebbecke [d], Jan Haubrich [d], Robert Hanelt [e]

[a] Institute of Structural Lightweight Design, Johannes Kepler University Linz, Altenbergerstr. 69, Linz, 4040, Austria
[b] Department of Aerospace Structures and Materials, Delft University of Technology, Kluyverweg 1, Delft, 2629 HS, Netherlands
[c] Department of Aerospace Science and Technology, Politecnico di Milano, Via La Masa 34, Milano, 20156, Italy
[d] Institute of Materials Research, German Aerospace Center, Linder Hoehe, Cologne, 51147, Germany
[e] INVENT GmbH, Christian-Pommer-Straße 47, Braunschweig, 38112, Germany

ABSTRACT

Modern aircraft structures consist of a multi-material mix, dominated by high-performance composites, but also including metal alloys, e.g., for load introduction parts.

This experimental research investigates the static and fatigue strength of pinned hybrid titanium-composite single-lap-shear joints. The Ti6Al4V adherend is manufactured by laser powder bed fusion. The joining is done by co-curing with the carbon fiber reinforced polymer adherend. The static tests focus on damage initiation and ultimate load, and are benchmarked by identical joints without pins. The fatigue tests focus on damage initiation and propagation. Digital image correlation is used for damage monitoring. Results show, (i) a high ratio of static ultimate failure to damage initiation load, (ii) early low-cycle damage initiation but then long high-cycle fatigue life until failure, and (iii) the crack stopping effect of the interlocking pins. Furthermore, visual joint failure analysis reveals a variety of damage modes, suggesting comprehensive testing and proper pin design.

1. Introduction

Large lightweight structures like civil aircrafts consist of a huge number of joined subcomponents and structural elements. Traditionally, joining between the different components is done by, e.g., riveting and bolting. For today's high-performance composite dominated aircraft structures, adhesive bonding is widely used due to its lower weight and advantageous load transfer. However, due to the high dependency of adhesive properties on the quality of the manufacturing process, the difficulty of inspection, and the generally poor damage tolerance properties, rivets and bolts are still required to provide a fail-safe function in adhesive joints. This often results in conservative, and thus, heavy, unsustainable, and uneconomic designs. Modern aircraft designs, especially for medium and long distance travel, consist of a multi-material mix that is dominated by high-performance composites like carbon fiber reinforced polymer (CFRP) due to their large weight saving benefits. Nevertheless, certain structures such as doorframes, hinges, flap mechanisms and other load-introduction parts are still metallic (aluminium and titanium alloys or, rarely, steels) components. Thus, the hybrid joining of composite structures with

metal structures is a key challenge of lightweight design. Adhesive bonding alone does not provide adequate properties. Therefore, novel technologies, like e.g., pretreatments of the bonded surfaces and mechanical interlocking elements have been and are being investigated to improve adhesive strength, aging resistance and damage tolerance of such hybrid metal-composite joints [1,2].

In particular, interlocking elements have been shown to significantly increase the static, fatigue and damage tolerance performance of adhesive joints. This was demonstrated in extensive experimental research on pinned composite-composite joints [3] and also on pinned hybrid metal-composite joints [4,5]. The maturing of additive manufacturing technologies, such as the laser powder bed fusion process, enables the processing of high quality aircraft alloys (e.g., TiAl4V) and opens up new possibilities for hybrid joints, as both larger, complex metal components and intricate interface details can be produced in the same process. In addition, the idea of interlocking elements forms a synergy with co-curing of the joint (pins have to penetrate the composite). Co-curing does not use an additional adhesive film for bonding, but instead uses the polymer matrix of the composite as the

---

adhesive, simplifying the manufacturing process and joint sizing, and enabling thin bond lines [6]. While this reduces the number of critical production steps and the bonding mass, it also requires more complex tooling and replaces the adhesive film material with a composite matrix material that is typically less suitable for high-strength and damage-tolerant joints [7]. Thus, pinned hybrid joints are still not used in the aircraft industry today.

However, due to the high potential of mechanically interlocking hybrid joining technology, numerous studies have been and are being conducted to demonstrate its advantages in terms of joint properties and to overcome current drawbacks such as economical and reliable manufacturing. For example, Parkes et al. presented comprehensive studies on the strength properties and damage behavior of a titanium-composite single-lap-shear (SLS) co-cured joint that is reinforced with pins that are additively manufactured onto a titanium adherend. They investigated different pin designs under static loading and demonstrated their reinforcing effect up to a factor of 6.5 (for the best pin design and a laser surface treatment), and furthermore, provided a profound failure analysis by the ultrasonic inspection technique under increasing load level and damage state [8]. For the same hybrid joint, specimens were also subjected to fatigue loading, showing typical strength behavior (logarithmic decrease in load cycles to failure with increasing load amplitude) and, most notably, a significantly slowed damage propagation phase after damage initiation. The damage propagation throughout the fatigue tests was investigated by the specimen elongation and two strain gauges. Both clearly show the initiation of a damage and its monotonic propagation with the number of load cycles [9]. Similar was investigated and found by Stelzer et al. for cold metal transfer welded pins [4,5]. However, they monitored the damage propagation along the bond line using a digital image correlation (DIC) system and concluded the damage modes occurring from the developing spatial strain distribution. Huelsbusch et al. [10] also investigated pinned titanium-composite joints. They used additive manufacturing for both, titanium adherend and pins and analyzed the influence of the pin size (in thickness direction) on the strength properties under quasi-static and low-cycle fatigue loading, thereby showing the positive effect of larger pins and assessed occurring damage mechanisms by post-test analysis of the fracture surfaces by scanning electron microscopy. A very fundamental experimental study on different pin designs was presented in [11], where it was demonstrated by pin pull-out tests that thin pins produce significantly less disturbances in the composite fiber alignment and pins with blocking features (e.g., a ball at the pin end) significantly increase the maximum pull-out load and energy. A model-based approach to analyze the potential of the interlocking pin shapes and sizes was done by [12], who used finite element based parametric optimization to find the optimal pin design on the level of a generic representative volume element with different loading. The numerical results were also validated by experimental pin pull-out tests, thereby showing a significant effect of the pin design on the static strength properties (+150% in maximum pull-out force and +720% in energy absorption to failure). For a more comprehensive research overview on hybrid joints with interlocking elements see, e.g., [12,13]. In conclusion, reliable hybrid joints with additively manufactured pin-like elements for additional mechanical interlocking, high strength and high damage tolerance between titanium and composite adherends are possible and have high potential for further improvement. Therefore, the SUSTAINair research project funded by the European Union's Horizon 2020 program investigated numerous hybrid joint designs as a key enabling technology for more sustainable aircraft designs.

This research investigates the static and fatigue performance of a co-cured pinned hybrid titanium-CFRP SLS joint over a wide load range. Details are provided on the manufacturing of Ti6A4V adherends by laser powder bed fusion and the joining with the CFRP adherends by co-curing. In total ten identical pinned hybrid joints were tested, two by static, and eight by tension-tension cyclic loading. Static results show a high ultimate load relative to the damage initiation load and are
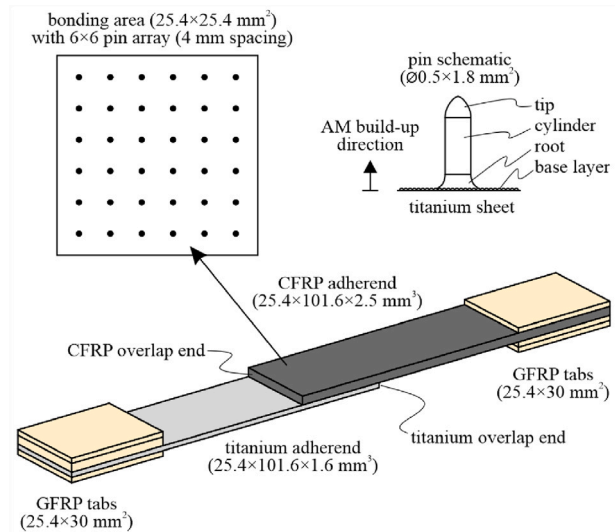

Fig. 1. Schematic of pinned hybrid titanium-CFRP SLS joint.

Fig. 2. Photographic image of pinned hybrid titanium-CFRP SLS joint.

benchmarked by available test results with identical specimens without pins. Fatigue results show early damage initiation in the low-cycle fatigue regime but then long further fatigue life until if fails in the high-cycle fatigue regime. Thus, the specimen shows large damage tolerance due to the interlocking pins. For damage initiation and propagation evaluation an efficient DIC-based evaluation method is proposed, that allows the detailed representation of the damage propagation and the crack stopping effect of the interlocking pins also for high-cycle fatigue tests. Joint failure analysis reveals a wide damage mode variety that suggests comprehensive testing and proper pin design.

2. Materials and methods

2.1. Test specimen and manufacturing

The tested pinned hybrid SLS joint specimen is presented in Figs. 1 and 2. The specimen geometry is based on ASTM D5868 [14]. The metallic adherend consists of a Ti6Al4V sheet strip (thickness 1.6 mm) that is covered in the bonding area by a single laser powder bed fusion base layer of Ti6Al4V. This design was selected to save manufacturing time and maintain the comparability of the joint test results with fully additively manufactured parts. The pin geometry is a simple spike shape with a diameter of 0.5 mm and a total height of 1.8 mm (75% of CFRP adherend thickness). Tip and root fillet ($r = 0.5$ mm) were designed for better fiber bundle opening and penetration into the CFRP

Table 1
Laser powder bed fusion process parameters used for pin manufacturing.

Parameter	Value	Unit
laser power	175	W
scanning velocity	500	m/s
hatch distance	40	μm
layer thickness	30	μm
energy density	117	J/mm^3
laser pattern	chess	
platform temperature	200	°C

adherend during co-curing, and the reduction of stress concentrations, respectively. The pins are arranged in the symmetric 6 × 6 pattern shown in Fig. 1. The present joint design is derived from the design and test results presented in [10]. Further development was done based on internal expertise and studies. The diameter was chosen to minimize fiber perturbation while maintaining sufficient pin stability to prevent kinking during the joining process and to enable a repeatable and accurate additive manufacturing process. The pin length was maximized while ensuring that the CFRP top layer was not punctured during joining. To emphasize the role of the pins in the failure behavior, surface pretreatment often used to improve adhesion and aging resistance was omitted.

2.1.1. Additive manufacturing of pin array

The pin array was additively manufactured onto a Ti6Al4V titanium sheet. Therefore, the sheet was chemically cleaned with acetone in an ultrasonic bath and subsequently checked for contamination with energy-dispersive x-ray spectroscopy in a scanning electron microscope. Next, the single-layer base (applied exclusively at bonding area) and the pin array were additively manufactured by laser powder bed fusion on a SLM 280^{HL} (provided by Nikon SLM Solutions AG), employing a 400 W Nd:YAG fiber laser. The powder used was ELI grade Ti6Al4V powder with a nominal powder size distribution of 15 to 45 μm (provided by Advanced Powders & Coatings). The laser powder bed fusion processes were carried out in an argon 5.0 atmosphere at a constant building platform temperature of 200 °C. A minimum layer-time of 30 s was chosen to avoid intrinsic heat effects on microstructure formation that are not present in larger structural components [15]. The build-up direction is indicated in Fig. 1. The titanium sheet was secured at the level top height with a custom fixture. A detailed powder analysis for the Ti6Al4V and the corresponding process parameter optimizations for bulk and contour are provided in previous works [16,17]. For manufacturing of the current pins, the parameters presented in Table 1, were employed (based on results in [16]). After manufacturing, the specimens were heat-treated at 900 °C for 2 h, which decomposes the as-built α martensite, forming an α-β microstructure [18].

2.1.2. Co-curing of the hybrid joint

For the co-curing process, the prepreg system HexPly®913C-926%-35% (provided by HEXCEL® Corp.) with a grammage of 577 g/m^2 was chosen as composite material. The prepreg consists of high-strength 6K carbon fiber roving with a density of 1.77 g/cm^3 that are woven into a 5H Atlas fabric with a grammage of 375 g/m^2. The thermoset matrix is epoxy based, has a density of 1.23 g/cm^3 and accounts for 35 wt-% of the material. A symmetric layup [0/90, ±45,0/90, $\overline{\pm45}$]$_S$ was used to reach the nominal CFRP thickness of 2.5 mm.

The hybrid joints were manufactured by INVENT GmbH (Braunschweig, Germany) using a hot press process. For this purpose, the dedicated press tool shown in Fig. 3 was developed. To manufacture the specimens in a first step, the press tool with cutouts for the titanium sheets was placed in the press bed. After inserting the titanium sheets (with pins), a two-part press frame was placed on top of the baseplate, leaving only the pin array accessible. Afterward, the prepreg layup was placed manually inside the frame. Special care was taken to push the pin array uniformly into the prepreg material. In addition, good
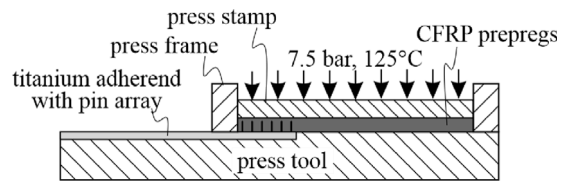

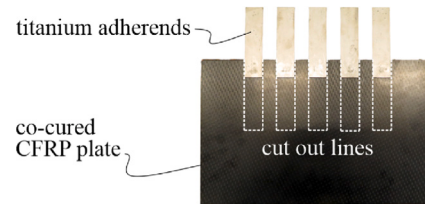**Fig. 3.** Co-curing press tool schematic.

Fig. 4. Semifinished part (for five specimens) after demolding with cut out lines.

sealing of the pressing tool was necessary to prevent the resin from leaking, and thus, ensure consistent laminate quality. In a last step, the press stamp was placed on top of the layup. The resin was cured for 1.5 h at a temperature of 125 °C and a pressure of 7.5 bar. Fig. 4 shows the semifinished part after demolding and cleaning of resin residues. Subsequently, GFRP tabs were adhesively bonded before the semifinished part was cut into batches of five specimens.

2.2. Experimental setup and procedure

The experimental setup is presented in Fig. 5, and consisted of hydraulic grips that are linearly guided by three massive columns with linear ball bearing guides, and a digital camera. The specimen was clamped by the hydraulic grips. Electrical contacts and piezoelectric sensors were attached to the specimen (see Fig. 5). These sensors were used for other test campaigns focusing on structural health monitoring, and are therefore not considered in the present study. The longitudinally loading was done by a 25 kN servohydraulic cylinder. The applied loads were, (i) a quasi-static load ramp (0.2 mm/min) with load holding periods (after every 1 kN load increase for approximately 30 min), and (ii) a cyclic tension-tension load ($R = 0.1$, 4 Hz). The load was measured by a 25 kN load cell at a sampling rate of 100 Hz. The spatial displacement and strain were measured by a DIC system (Vic-2D 6, provided by Correlated Solutions Inc.). The DIC was also used for damage evaluation. Therefore, photographic images of the side of the pinned hybrid SLS specimen were taken, (i) every second during static tests, and (ii) at each 16th load cycle maximum during cyclic tests. The observed side of the specimens was coated by a white primer and a black random speckle pattern (typical image see Fig. 5). The digital images were taken with 5 MP and 280 mm focal length. The camera distance was approximately 120 mm. The DIC was done by a subset size of 63 px and a step size 16 px, i.e., it evaluated approximately in a 0.21×0.21 mm^2 grid and the evaluated area is approximately 0.84×0.84 mm^2.

2.3. Continuous damage evaluation by digital image correlation

The pinned hybrid SLS specimens were evaluated for damage initiation and propagation until failure by using the continuously taken DIC images (see, Fig. 5). The damage evaluation was done based on the change in the principal strain along the bondline. The reference image was taken at the initial state. When a crack propagates into an evaluated DIC subset, the bonded surfaces separate and open (due to joint rotation). This is interpreted by the DIC evaluation as a large strain, and is a sensitive indicator for a crack [4,19]. Additionally to
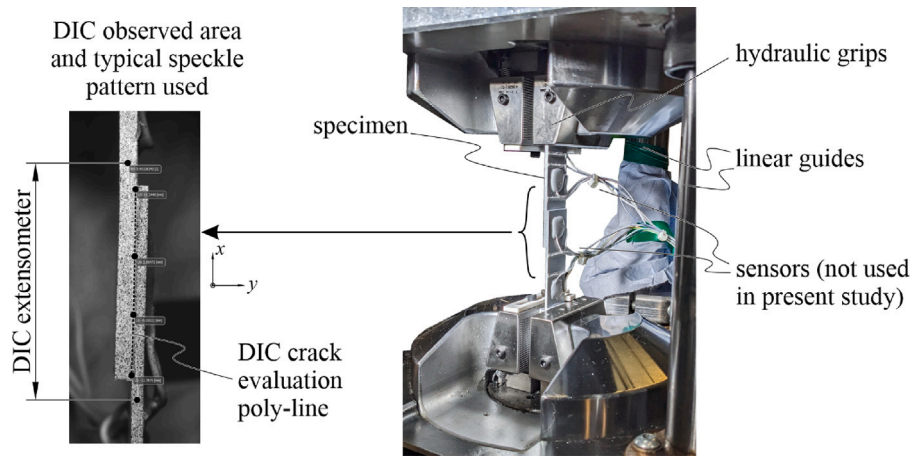
Fig. 5. Experimental setup and example of typical DIC image with speckle pattern, poly-line used for damage evaluation, and extensometer spots used to calculate the average normal strain.

Table 2
Results of static tests.

Result	Damage location	Unit	Specimen no.	
			81	90
static load at damage initiation	titanium end	kN	4.0	3.9
	CFRP end	kN	4.7	5.0
static load at ultimate failure		kN	9.0	10.4
crack length before failure	titanium end	mm	8.6	9.7
	CFRP end	mm	6.5	8.9
DIC evaluation threshold		μ-strains	4348	5380

the principal strain, also the correlation confidence of DIC was tested for damage evaluation (according to the method presented in [20]). The latter was found to be more prone to measurement noise. However, the method is limited in its crack length resolution by the DIC step size and towards the overlap ends by the subset size.

Other than in [4], the present work used a threshold value on the principal strains measured by the DIC system to identify damage in a subset. Furthermore, the strains were exclusively evaluated at a poly-line that was defined along the specimen bondline (see exemplary in Fig. 5). To find the threshold values, for both static and fatigue tests, the strain distribution change along this poly-line (bondline) is evaluated with respect to the loading (sudden strain changes indicate damage). This enabled the efficient and automated damage evaluation for all DIC images taken throughout a test. The basic assumptions that the damage initiates at the stress concentrations at the adherend overlap ends and further develops along the bondline until the final rupture is well supported by literature and previous results of the authors [8,13,20]. Moreover, the bondline crack was assumed to develop rather quickly over the width of the specimen, and thus, the observation of one side of the pinned hybrid SLS specimen was considered adequate to monitor the damage initiation and propagation.

3. Results and discussion

The tested pinned hybrid SLS specimens are part of a larger test campaign. The ten specimens tested for the present research are designated SLS81 through SLS90. SLS81 and SLS90 were tested by static loading. SLS82 through SLS89 were tested by cyclic loading.

3.1. Static test results

The static test results are summarized in Table 2, including the principal strain thresholds used for DIC-based damage initiation evaluation. For further analysis and better comparability to other studies with differing bond dimensions, Fig. 6a shows the stress–strain results

of the statically loaded pinned hybrid SLS specimens. The stress is the average shear stress over the bonding, given by the crosshead loading and the pristine bonding area ($25.4 \times 25.4\,mm^2$, i.e., the average shear stress does not reflect the true stress increase in the bondline when damage propagates). The strain is the average strain over the defined DIC extensometer (cf. Fig. 5). The stiffness behavior of the specimens is initially linear. Also load holding periods after every 1 kN of load-increase did not affect this behavior (cf. measurement data point accumulations at 1.55 and 3.1 MPa before first damage initiation at 6 and 6.2 MPa, respectively). After first damage initiation, specimen stiffness began to decrease with increasing load. Furthermore, stiffness degradation during load holding periods indicated damage propagation without load increase (cf. average shear stresses drop at 7.8, 9.3, 10.8 12.4, 14.0 and 15.5 MPa). The SLS81 even failed during a load holding period. Fig. 6b shows exemplary the DIC principal strain evaluations of SLS90 for the first damage initiation (titanium adherend overlap end) at 3.9 kN tensile load (6 MPa average shear stress), the second damage initiation (CFRP adherend overlap end) at 5 kN tensile load (7.7 MPa) and a propagated damage at 8 kN tensile load (12.4 MPa). The damage evaluation thresholds were found by observing the load-normalized local principal strains along the bond line. Initially, the normalized strain distribution showed little change with increasing load (changes were assumed to be mainly driven by the geometric nonlinear effect of joint rotation). The first sudden and disproportionate strain deviation from the initial distribution was considered to be indicative of damage initiation (found to always be very local at the overlap ends). The threshold for further damage propagation evaluation was set between the highest strain value before and the highest strain value after the sudden strain deviation (values see Table 2). Due to the adherend stiffness imbalance the highest strain was always at the titanium adherend overlap end, where also the first damage initiation took place for both specimens. However, with further load increase a second damage initiated at the CFRP adherend overlap end and the initiated damages propagated until final failure of the specimens. This was found to be similar for both samples (cf. Table 2) and shows a large
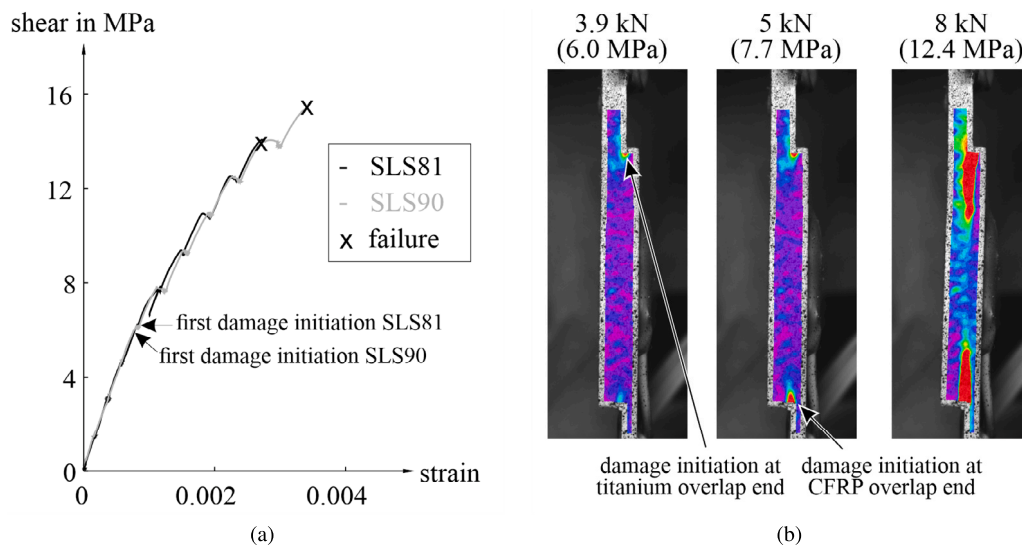
Fig. 6. (a) Average shear stress over average strain results of static tests with specimens SLS81 and SLS90, and (b) DIC principal strain evaluation results of SLS90 for damage initiation loads (3.9 kN/6 MPa and 5 kN/7.7 MPa) and a load (8 kN/12.4 MPa) with propagated damage (red: value ≥ DIC evaluation threshold).
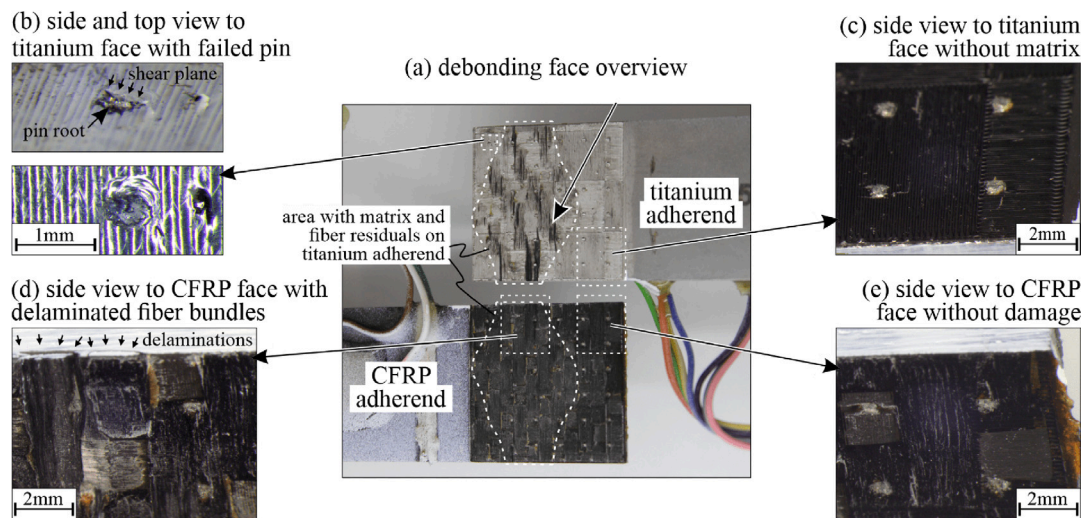

Fig. 7. Photographic images of debonded adherend faces of static loaded specimen SLS81, (a) overview, (b) typical example for pin failure, (c and e) adhesive failure dominated debonding faces, and (d) cohesive failure dominated detail with delaminated fiber bundles.

mean load increase factor between damage initiation and final failure of 2.5. For benchmark, four identical hybrid titanium-CFRP SLS specimens without pins were tested at the laboratory of the TU Delft. These show a mean damage initiation load of 3.6 kN with a standard deviation of 0.4 kN (5.5 and 0.7 MPa average shear stress, respectively; the load was determined on the basis of discontinuities in the load–displacement curve) and a mean ultimate load of 4.6 kN with a standard deviation of 0.4 kN (7 and 0.6 MPa average shear stress, respectively). The pins therefore only have a minor influence on the load that initiated the damage, but maintained the strength and the stiffness of the damaged joint and allowed the load to be increased twice as much until the final failure.

However, the typical initial damage mechanisms reported in the literature are a bondline failure of the polymer matrix (i.e., cohesive failure) or, a separation of the adherends along the joint interface (i.e., adhesive failure: bond breaking at the metal-polymer or metaloxide-polymer interface) [21]. Which of the two mechanisms initiated at the present specimens cannot be identified clearly with the given analysis tools. However, the exemplary photographic images of the debonded adherend faces of SLS81 presented in Fig. 7a, c and e

suggest adhesive failure as the predominant failure mode until final rupture at crack lengths of 8.6 mm (titanium overlap end) and 6.5 mm (CFRP overlap end), respectively (according to the threshold-based DIC evaluation). At the area of the final rupture residuals of matrix and fiber bundles were found on the titanium adherend, and fiber bundles delaminated at the CFRP adherend side (cf. Fig. 7a and d). Thus, for the final rupture a failure mode change to cohesive failure was found. A similar cohesive-adhesive bondline failure and large load carrying capacity after damage initiation was also found in a previous work [20] for a comparable SLS specimen and a low number of quasi-static, tension-tension load cycles. Further analysis of the statically tested specimens SLS81 and SLS90 showed that regardless of the failure mode of the adhesive layer, all pins failed at the cylindrical part. The pin failure plane was inclined to the bonding plane. In the adhesive failure zone they failed close to the root. One failed pin is exemplary shown from the side and the top in Fig. 7b. A result that was also reported by [22] for purely shear loaded pinned hybrid joints. Some of the pins within the area of matrix and fiber remnants on the debonded face (cohesive failure dominated) were also slightly longer and the failure plane was also steeper. This suggests an increasingly important role of

Table 3
Results of fatigue tests.

Result	Unit	Specimen number							
		84	85	86	87	88	89	82	83
Cyclic peak load	kN	4	3	3	2.5	2.5	2.25	2	1
	%	102	76	76	64	64	57	50	25
Damage initiation	k-cycles	0.18	0.58	0.29	0.38	0.74	4.19	29.7	–
DIC eval. threshold	µ-strains	3718	2948	8794	7333	5383	1974	2000	5385
failure	k-cycles	12.1	97.0	55.0	214.2	147.7	758.3	1150	–

Table 4
Fatigue result fitting parameters (k, d), standard deviation (SD) and coefficient of determination (r^2) for fatigue results of specimens SLS84 to SLS89.

Result	k	d	SD	r^2
damage initiation	4.2229	4.6599	0.30	0.79
failure	6.5226	7.9746	0.15	0.97

axial loading of the pins for a propagated debonding state. However, the cylindrical part always remained in the CFRP adherend. In the area dominated by adhesive failure, the pin-enclosing CFRP face material showed no observable damage on the analyzed scale (cf. Fig. 7e).

3.2. Fatigue test results

The applied cyclic peak loads were between 25% and 102% of the averaged static damage initiation load (i.e., 3.95 kN), respectively. Table 3 summarizes the results of the fatigue tests. For the pinned hybrid SLS specimen cyclic loaded by 25% of the averaged static damage initiation load, the test was stopped after 10^6 cycles without any damage being detected. For the specimen cyclic loaded by 50% of the averaged static damage initiation load adherend debonding initiated after $29.7 \cdot 10^3$ cycles (CFRP overlap end) and $6.5 \cdot 10^5$ cycles (titanium overlap end), and developed from both sides until the first pin row, where both cracks got arrested until at $1.15 \cdot 10^6$ cycles the titanium adherend itself failed due to a fatigue crack. The fatigue crack had developed normal to the loading within the Ti6Al4V sheet. It initiated at the transition of the additively manufactured ground layer to the pin roots. For all other cyclic loaded specimens with loads ≥57% of the averaged static damage initiation load, the damage propagated faster and further through the bondline and its pins. Thus, for very low loads and a very high number of cycles a damage mode change occurred after damage initiation and arrival at the first pin row. Fig. 8 shows the failed specimen including details of the fatigue crack initiation at the titanium adherend at an arbitrary pin. However, since aircraft design typically considers a maximum of 10^6 load cycles and the present research focuses on the bonding properties, only the six specimens loaded ≥57% of the averaged static damage initiation load were used for the further analysis. Both, fatigue damage initiation and failure for the six considered specimens are presented in Fig. 9. The exact cycle numbers and the principal strain thresholds used for the DIC-based damage evaluation are summarized in Table 3. These threshold values were found by the strain distribution change along the bondline that occurs when a damage initiates (all DIC images are taken at the cycle's peak load; the varying value magnitudes can be explained by the manual definition of the DIC evaluated poly-line). However, due to measurement noise (typical signal-to-noise ratio for cyclic loading is in the magnitude of 12 dB; no additional filtering was applied), a margin was built into the thresholds to prevent premature exceeding. Thus, the threshold values for the fatigue loaded SLS specimens were found by increasing the threshold value (in steps of 2%, starting with the maximum strain along the bondline in pristine condition) until a damage initiation different from the first few cycles was found.

For the six specimens that featured bondline failure, the relation between peak load $(R = 0.1)$ and cycles until damage initiation

and final failure, respectively, were considered to be of the classical exponential form $f = cn^{-1/k}$, where f is the cyclic load, n is the number of cycles and c, k are the fitting parameters. This relation can be rewritten in the double-logarithmic domain for cycles until damage initiation and final failure by $\log(n) = d - k \log(f)$, where $d = k \log(c)$. The fitting parameters k and d were found for $p = 50\%$ probability of occurrence by a least-squares-fit with respect to the cycle numbers of the six considered specimens (log-normal distribution of the measurement values was assumed) [23]. The calculated fitting parameters, the standard deviations of the residuals and the coefficients of determination for both damage initiation and final failure are presented in Table 4. Both fitted functions show a reasonable standard deviation and coefficient of determination and are plotted in Fig. 9. The final failure cycle numbers scatter significantly less and show a much higher coefficient of determination than the damage initiation cycle numbers. This larger scatter of the damage initiation results may be explained by, (i) its susceptibility to manufacturing imperfections, and (ii) the difficult determination of the moment of the first damage initiation, in particular, as only one side of the SLS specimens is observed by the DIC system. However, it may be discussed if a cyclic load close at the static damage initiation load can be considered a fatigue load. Nevertheless, the fitted function correlates the results well and furthermore enables to investigate the transition between static and fatigue loading. Generally, all load levels showed damage initiation at low cycle numbers. This also applied to comparatively low peak loads.

In contrast, further damage propagation to final specimen failure required high cycle numbers. This is true for all six considered test specimens. Thus, compared to the fatigue life until damage initiation, the pinned hybrid joint features an extremely long fatigue life until final failure. This is also true for a load level at the static damage initiation load. A similar finding was made by [9], however, the pinned hybrid SLS joint investigated in the current work exhibits a much longer fatigue life after damage (for comparable cycles to final failure, the ratio between the number of cycles to failure and damage initiation is approximately 10 times larger). This large difference may be partly a result of the potentially more sensitive damage initiation evaluation method used in the present work, but clearly suggests a well-designed pin shape and array. Furthermore, Fig. 10 shows the development of the damage represented by the total crack length (sum of crack length at the CFRP and the titanium overlap end) over the load cycles. The lifetime is normalized by the number of cycles at final failure for better comparability of the damage propagation between the considered six specimens. The plotted crack length developments differ from each other, however, they show a clear trend to a fast damage propagation directly after initiation, followed by a comparatively long and moderate propagation phase before the propagation becomes over-proportional towards the final failure. Furthermore the final damage size decreases with the loading between 57% and 76% of the averaged static damage initiation load which is plausible. From 76% to 102% of the averaged static damage initiation load, this trend is not clear and would require further testing to achieve reliable conclusions. In summary, it may be stated that the normalized damage propagation behavior shows similar trends for all loads considered. Therefore, it could be assumed that the mechanisms that propagated the damage were also similar.
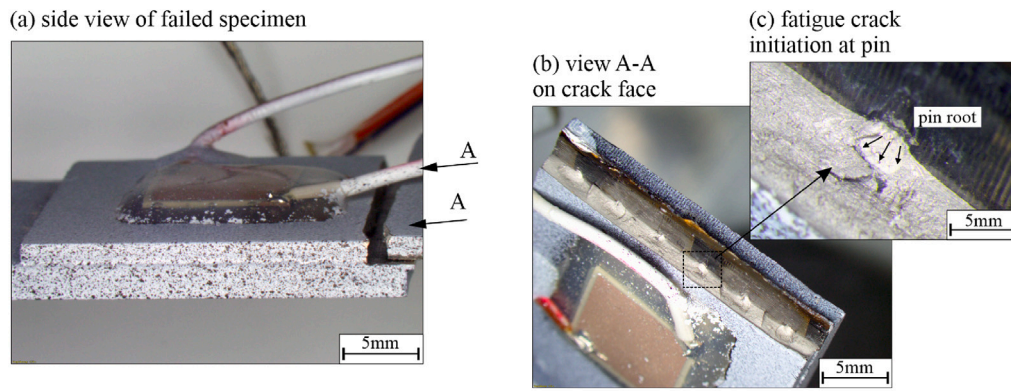
(a) side view of failed specimen

(b) view A-A
on crack face

(c) fatigue crack
initiation at pin

pin root

5mm

5mm

Fig. 8. Photographic images of SLS specimen fatigue loaded by 50% the averaged static damage initiation load, (a) side view with damage propagation path, (b) overview on crack face, and (c) exemplary titanium adherend fatigue crack initiation at arbitrary pin.
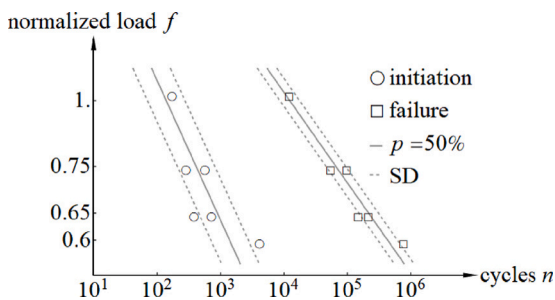

Fig. 9. Fatigue damage initiation and failure results for SLS84 to SLS89 and exponential fitting function ($p = 50\%$) with standard deviation (SD).
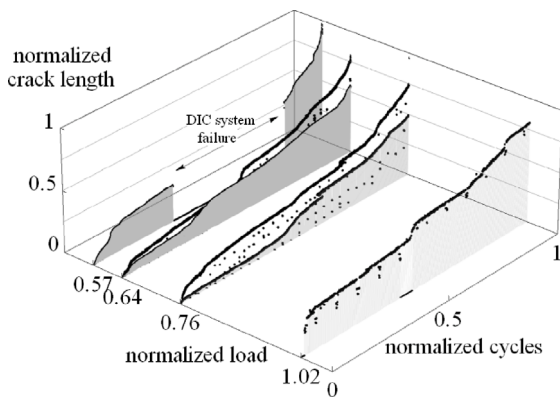

Fig. 10. Fatigue damage propagation over number of load cycles until failure for SLS84 to SLS89 (DIC evaluated at every 16th load cycle; normalized by the overlap length and the cycles to failure, respectively).

This assumption is also supported by the photographic images of the debonded faces presented in Fig. 11. Until final joint rupture the debonding propagation of all six SLS specimens was dominated by adhesive failure (i.e., CFRP matrix separated from titanium). For load levels at and above 76% fatigue load at the area of final rupture some of the CFRP matrix and fibers remained on the titanium adherend (cohesive failure mode). Independent of the bonding failure, all pins ruptured and remained in the CFRP. However, a closer look at the debonded surface also showed different pin failure modes. While the pins at the adhesively failed bonding featured fatigue cracks at different locations, the pins at the cohesively failed bonding ruptured at their shaft. These different failure modes and planes of the pins may be explained by the different loads to which the pins were subjected to when the debonding crack faces separated. This separation of the crack

faces is driven by the load introducing adherend's elongation (crack face sliding) and curvature (crack face opening), both of which depend on the load and the debonding progress and may be represented by the joint rotation. Fig. 12 schematically shows three pin loading scenarios and Fig. 13 exemplary shows photographic images of resulting pin failure modes.

Pin load scenario I is characterized by small overlap end debonding and joint rotation, which results in a pin load F_P, which is predominantly transverse $F_T \approx F_P$. Subsequently, the pin is double-curved due to its embedding and fatigue crack can initiate at the locations of the maximum normal stresses (pin root and shaft at transition to CFRP). However, due to the compliant embedding of the pin in the CFRP and the superimposed stresses of the titanium adherend itself, the root crack is believed to dominate initially. This root crack was found to typically propagate into the adherend material, where it is assumed that is slowed down. As a result of the root crack a load transfer to the shaft takes place, where the fatigue crack could propagate unhindered until final rupture. Fig. 13 shows two examples of pin failure under assumed load scenario I. In particular the first pin row at the titanium overlap end supports the proposed failure evolution, as it shows two fatigue cracks and a remaining pin fragment. This pin failure behavior was only found in the outer pin rows of the low loaded specimens (57–62% of the averaged static damage initiation load).

Pin load scenario II is characterized by medium overlap end debonding and joint rotation, which results in a pin load F_P, which is transverse F_T and increasingly axial F_A. For the resulting double-curved pin, again the root crack is believed to dominate initially. However, before the shaft crack could develop again, the pins were teared out from the titanium adherend by the existing axial force. Fig. 13 shows three examples for pin failure under load scenario II. This pin failure behavior was found for all fatigue tested specimens that featured bondline failure. It dominated until final rupture of the specimens.

Pin load scenario III is characterized by large overlap end debonding and joint rotation, which results in a pin load F_P, which is transverse F_T and axial F_A. At this scenario the pin load is typically also significantly higher due to the advanced damage state. As a result, the pin is overloaded, yields, and ruptures in its critical stress plane. This rupture plane is oriented opposite to the fatigue cracks and is located on the shaft at the transition to the CFRP or, at higher loads, slightly inside the CFRP. Fig. 13 shows one example for pin failure under load scenario III. This pin failure behavior was found for all fatigue tested specimens that featured bondline failure. It dominated during final rupture of the specimens.

Thus, during the propagation of the debonding the pin failure behavior changed due to the changing local loading of the pins. This sequence of pin loading (scenarios I to III) and corresponding failure modes is dependent on the extent of damage and load severity and was exhibited by all specimens considered (higher loaded specimens started
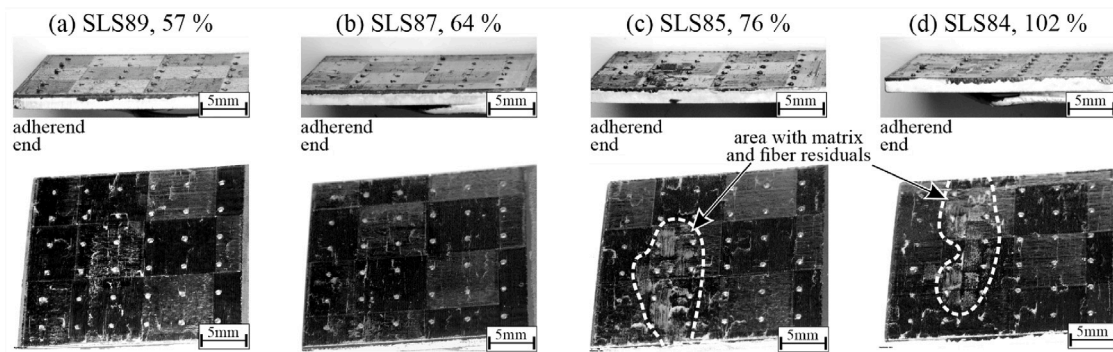
Fig. 11. Photographic images of debonded titanium adherend faces of SLS specimens fatigue loaded by (a) 57%, (b) 64%, (c) 76%, and (d) 102% of the averaged static damage initiation load.
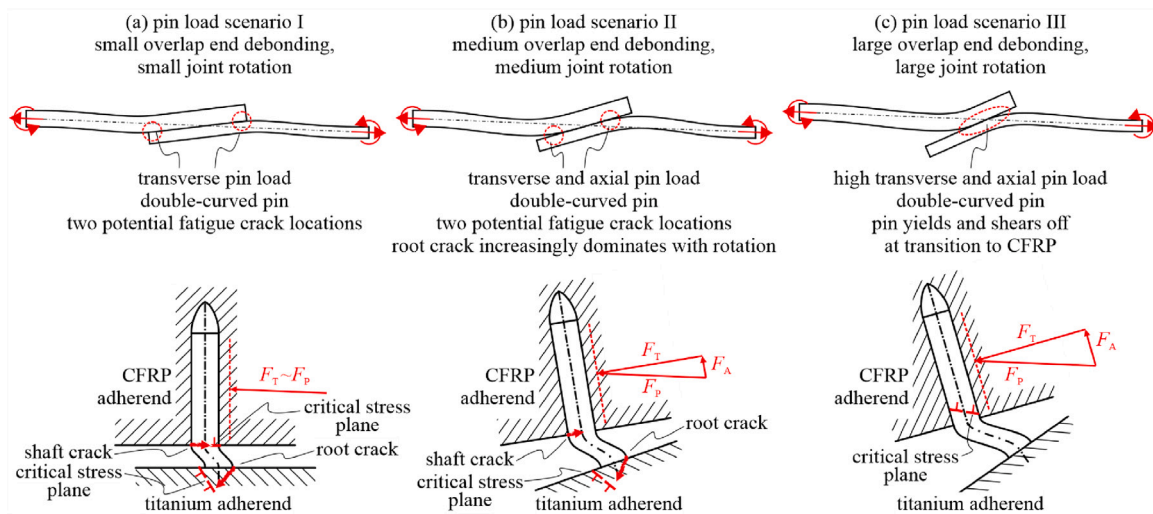

Fig. 12. Pin load scenarios for, (a) small overlap end debonding and joint rotation, (b) medium overlap end debonding and joint rotation, and (c) large overlap end debonding and joint rotation.
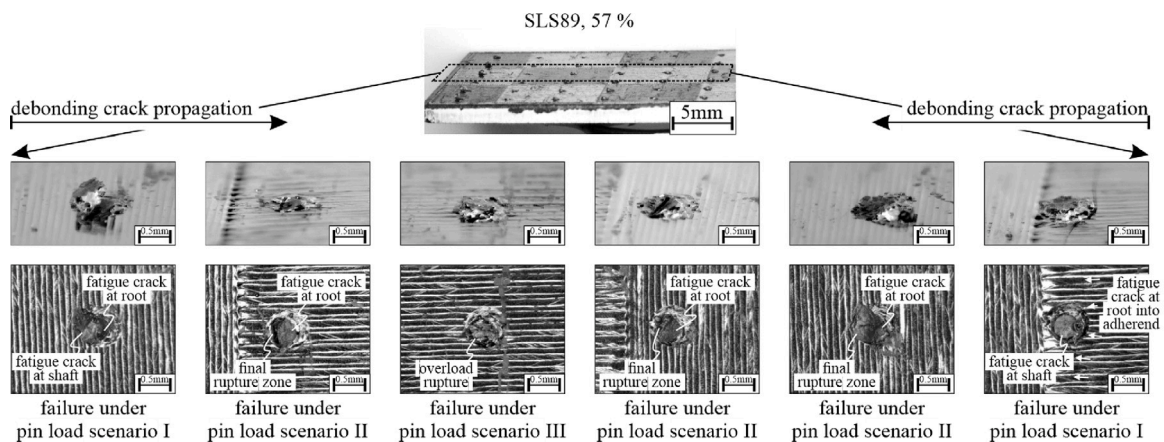

Fig. 13. Photographic images of pin failure of SLS specimen fatigue loaded by 57% of the averaged static damage initiation load and the assumed pin load scenarios.

with pin loading scenario II). These results were found to correlate well with the findings of [9] for a similar pinned hybrid SLS specimen. In addition, the two failure modes of cohesive debonding and inclined pin shaft rupture due to overload (which were found for the final rupture of the fatigue tested specimens) are also found for the statically tested specimens. Therefore, it is expected that as the cyclic loading increases, the failure behavior of the specimens under fatigue will show a smooth transition to the failure behavior under static loading. Hence, it may

also be expected that the high residual strength potential found for statically loaded specimens may also be present for fatigue-damaged specimens. Furthermore, for the low fatigue loaded specimen presented exemplary in Fig. 13, beginning adherend fatigue cracks that initiate at the roots of the right pin row were found. Thus, a further reduction of the cyclic load would not significantly increase the specimen lifetime but simply result in the failure mode presented in Fig. 8 for the specimen loaded by 50% of the averaged static damage initiation load.
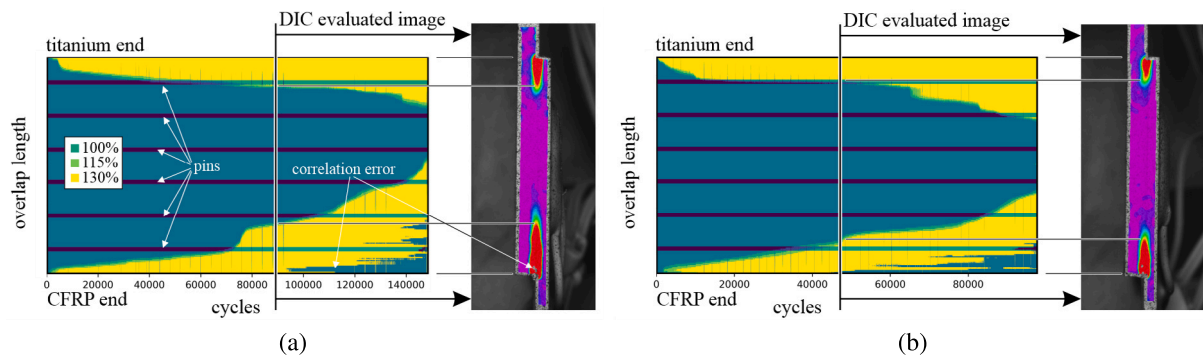
Fig. 14. SLS debonding crack propagation over load cycles evaluated by DIC principal strain thresholds of specimens loaded by (a) 0.64%, and (b) 0.76% of averaged static damage initiation load; color shading in DIC image represents principal strain (red: value exceeds threshold); color shadings in damage propagation plots represent a value higher that 100%, 115%, 130% of the strain threshold.

This demonstrates a large damage tolerance of the investigated pinned hybrid SLS specimen for different loading regimes. This is an advantageous property for structural applications, and was assigned to be a direct effect of the pin array by researchers [4]. However, the pin rows did not only slow down the propagation of the crack in the bondline but also caused a distinctive propagation pattern. This could be visualized by the used continuous, high-frequency damage monitoring by DIC. Fig. 14 illustrates the found effect of the six rows of pins (six pins per row perpendicular to the loading direction, cf. Fig. 1) for two of the SLS specimens tested. Every pin row slowed down the damage propagation whenever one was reached. After a pin row was overcome by the debonding crack, presumably by failure of all pins of a row, another stage of fast damage propagation took place, which then was again slowed down significantly when a subsequent pin row was reached. Deviations of pin row positions and damage propagation slowing are expected to be rooted in the specimen width and the DIC debonding crack length evaluation from only one side, as the front line of the debonding crack is expected to be not perfectly straight and not perfectly perpendicular oriented. However, with the debonding crack size the number of cycles required to overcome a pin row became less (cf. Fig. 14). This reduction of cycles to overcome a pin row is assumed to be a result of the increasingly disadvantageous pin loading presented in Fig. 12. However, further testing and analysis would be required to separate the effect of the increasing pin loading amplitude from the effect of the changed loading situation (bending as well as lateral and axial loading). The found two-stage failure pattern, i.e., fast pure bondline failure and slower mixed pin and bondline failure, was observed for all six considered fatigue loaded specimens.

3.3. Suitability of the digital image correlation-based damage evaluation

The proposed DIC and threshold-based evaluation may be less accurate than classical optical microscopy crack monitoring methods, but it allows continuous, high-frequency monitoring of damage initiation and propagation during long fatigue tests. In the present research, the crack length resolution is theoretically limited to 0.21 mm due to the used DIC step size and the overlap ends cannot be evaluated below the half subset size (0.42 mm).

More critical for the results may be the influence of the selected threshold values used to evaluate the principal strains. The method seems generally sensitive to damage onset, as the thresholds were found individually for every specimen by strain deviations from its pristine condition. However, this comes with the danger that the damage evaluation was influenced by the selected threshold or corrupted by measurement noise. To identify the threshold dependency, three different thresholds were used (the defined value and two higher ones: 115% and 130%). The results clearly show the expected influence (shorter crack lengths for larger threshold values) of the changed thresholds (cf. Fig. 14). However, when compared to the evaluated cycle numbers the

threshold effect is negligibly small. When compared to the evaluated crack lengths the effect is larger and appears to be rather independent from the absolute crack size. In the present study, the dependence of the crack length evaluation with a threshold variation of 30% was below 1 mm, which is considered appropriate. Furthermore, the evaluated propagation of the debonding cracks was continuous and monotonic over the entire lifetime of the fatigue tested specimens, thus, the influence of the measurement noise can be neglected.

Another effect that may lead to an overestimation of the crack length is the change in the strain distribution due to the reduction of the bondline (strain concentrations used to identify the crack tip, increasingly expand into the remaining intact bondline). Consequently, also intact bond behind the debonding crack tip could be identified as damaged by the defined threshold. This effect could not be reliably estimated. But considering the found correlation of damage propagation slowdowns and pin row positions shown in Fig. 14a up to a very advanced damage situation, it can also be assumed to be a small source of error.

However, considering the bonding length of 25.4 mm and the detailed, continuous and monotonic crack propagation results, the proposed DIC and threshold based evaluation method was found to be well suitable to monitor the effect of the pins on the damage propagation in the bondline.

4. Conclusions

The present research provides comprehensive static and fatigue results of a co-cured pinned hybrid titanium-CFRP SLS joint over a wide load range. The pin array is manufactured onto a titanium sheet of the same material by laser powder bed fusion. The hybrid joint is manufactured by co-curing of the CFRP adherend on the titanium pin array.

Static test results show a high ratio between ultimate load and damage initiation load (approximately 2.5). Furthermore, the pins seem to slightly increase the damage initiation load and to significantly increase the ultimate load compared to benchmark specimens without pins. The failure mode for the static loaded specimens is adhesive/cohesive bondline failure and pin shaft rupture. Damage initiation was at the joint overlap end with the higher stiffness imbalance. Fatigue test results cover a wide load level range and show failure modes that vary from adherend failure at low loads (50% of average static damage initiation load) to adhesive/cohesive bondline failure and pin shaft rupture at high loads (102% loading). For the lowest cyclic load (25% loading) no damage initiation was found until 10^6 cycles. All further fatigue tested specimens show an early damage initiation in the low-cycle fatigue regime and a long further life until final failure in the high-cycle fatigue regime. All damages initiated at the overlap ends of the bondline. During the first stable fatigue damage propagation phase the debondings were found to be dominated by adhesive failure and

pin fatigue cracking. The finally ruptured debonding faces also showed cohesive bondline failure and pin shaft rupture due to overloading. The pin failure modes varied with load and debonded crack length, and were attributed to joint overlap rotation and its correlated change in load on the bondline and pin. The failure modes during final rupture after fatigue loading are found to be similar to the failure modes for static loading.

The proposed continuous, high-frequency DIC-based damage evaluation method enabled to explicitly assign the crack stopping effect of the interlocking pin array to the long post-damage fatigue life. The method was discussed and shown to be suitable for the drawn conclusions. Furthermore, it allows the effect of individual pin rows on debonding propagation to be studied even in long fatigue tests, and thus, may be of great value for more detailed analysis of pin design effects in the future.

In conclusion, the pin array design of the investigated pinned hybrid SLS specimen seems to be well balanced, as the specimen featured numerous damage modes for different load levels. Applying further state-of-the-art measures to increase the adhesive strength of the bonding is highly expected to result in, (i) a longer undamaged fatigue life at the same time with a sufficient post-damage fatigue life, and (ii) a higher damage initiation load and a lower (but sufficiently high) damage initiation to failure ratio for static loading. Thereby, the used high-performance materials can be further exploited. However, optimization of the joint design must include the adherends, the adhesive layer and the pin shape and array, and the entire manufacturing process. Thus, future research needs to increasingly shift from a test-based design approach to a model- and optimization-based design approach in order to exploit the full potential of this promising joining technology.

CRediT authorship contribution statement

Christoph Kralovec: Writing – review & editing, Writing – original draft, Visualization, Validation, Project administration, Methodology, Investigation, Funding acquisition, Formal analysis, Conceptualization. **Andreas Dengg:** Writing – review & editing, Visualization, Methodology, Investigation, Formal analysis, Data curation. **Martin Schagerl:** Writing – review & editing, Supervision, Resources, Project administration, Funding acquisition, Conceptualization. **Arne Schiller:** Writing – review & editing, Methodology, Investigation, Formal analysis, Data curation. **Chiara Bisagni:** Writing – original draft, Supervision, Resources, Project administration, Funding acquisition, Conceptualization. **Miriam Loebbecke:** Writing – review & editing, Writing – original draft, Resources, Methodology, Conceptualization. **Jan Haubrich:** Writing – review & editing, Writing – original draft, Resources, Project administration, Methodology, Funding acquisition, Conceptualization. **Robert Hanelt:** Writing – review & editing, Writing – original draft, Resources, Project administration, Methodology, Conceptualization.

Declaration of competing interest

The authors declare that they have no known competing financial interests or personal relationships that could have appeared to influence the work reported in this paper.

Acknowledgments

Data availability

The authors do not have permission to share data.

References

[1] Ucsnik S, Scheerer M, Zaremba S, Pahr DH. Experimental investigation of a novel hybrid metal-composite joining technology. Composites A 2012;41:369–74. http://dx.doi.org/10.1016/j.compositesa.2009.11.003.

[2] Löbbecke M, Bayerbasi TJ, Bartsch M, Haubrich J. Role of surface structures on long term stability of adhesive joints between Ti-15V-3Cr-3Sn-3Al and polyether-ether-ketone. Int J Adhesion Adhesives 2023;120:103282. http://dx.doi.org/10.1016/j.ijadhadh.2022.103282.

[3] Bisagni C, Furfari D, Pacchione M. Experimental investigation of reinforced bonded joints for composite laminates. J Compos Mater 2018;52(4):431–47. http://dx.doi.org/10.1177/0021998317708021.

[4] Stelzer S, Ucsnik S, Pinter G. Fatigue behaviour of composite–composite joints reinforced with cold metal transfer welded pins. Int J Fatigue 2015;81:37. http://dx.doi.org/10.1016/j.ijfatigue.2015.06.004.

[5] Stelzer S, Ucsnik S, Pinter G. Strength and damage tolerance of composite-composite joints with steel and titanium through the thickness reinforcements. Composites A-Appl Sci Manuf 2016;88:39. http://dx.doi.org/10.1016/j.compositesa.2016.05.020.

[6] Wahab MA. Joining composites with adhesives: theory and applications. Destech Publications, Inc.; 2016.

[7] Vassilopoulos AP. Fatigue and fracture of adhesively-bonded composite joints. (52). Elsevier; 2015.

[8] Parkes PN, Butler R, Meyer J, De Oliveira A. Static strength of metal-composite joints with penetrative reinforcement. Compos Struct 2014;118:250–6. http://dx.doi.org/10.1016/j.compstruct.2014.07.019.

[9] Parkes PN, Butler R, Almond DP. Fatigue of metal-composite joints with penetrative reinforcement. In: Proceedings of the 54th AIAA/aSME/ASCE/AHS/aSC structures, structural dynamics, and materials conference. Boston, Massachusetts, USA; 2013, p. 1879. http://dx.doi.org/10.2514/6.2013-1879.

[10] Huelsbusch D, Haack M, Solbach A, Emmelmann C, Walther F. Ti-CFRP hybrid structures produced by laser additive manufacturing. In: Proceedings 20th international conference on composite materials ICCM-20. Denmark: Copenhagen; 2015.

[11] Sarantinos N, Kostopoulos V, Vita G, Campoli G, Bricout L. Enhancing the robustness of hybrid metal-composite connections through 3D printed micro penetrative anchors. Appl Compos Mater 2024;1–19. http://dx.doi.org/10.1007/s10443-024-10224-1.

[12] Sarantinos N, Kostopoulos V, Vita G, Campoli G, Bricout L. Micro-pins: The next step in composite–composite and metal–composite joining. CEAS Space J 2019;11:351–8.

[13] Graham DP, Rezai A, Baker D, Smith PA, Watts JF. The development and scalability of a high strength, damage tolerant, hybrid joining scheme for composite-metal structures. Composites A 2014;64:11–24. http://dx.doi.org/10.1016/j.compositesa.2014.04.018.

[14] ASTM D5868-01: Standard test method for lap shear adhesion for fiber reinforced plastic (FRP) bonding. 2014.

[15] Barriobero-Vila P, Gussone J, Haubrich J, Sandlöbes S, Da Silva J, Cloetens P, et al. Inducing stable $\alpha + \beta$ microstructures during selective laser melting of ti-6al-4V using intensified intrinsic heat treatments. Materials 2017;10:268–82. http://dx.doi.org/10.3390/ma10030268.

[16] Kasperovich G, Haubrich J, Gussone J, Requena G. Correlation between porosity and processing parameters in TiAl6V4 produced by selective laser melting. Mater Des 2016;105:160–70. http://dx.doi.org/10.1016/j.matdes.2016.05.070.

[17] Artzt K, Mishurova T, Bauer P-P, Gussone J, Barriobero-Vila P, Evsevleev S, et al. Pandora's box–Influence of contour parameters on roughness and subsurface residual stresses in laser powder bed fusion of Ti-6Al-4V. Materials 2020;13:3348. http://dx.doi.org/10.3390/ma13153348.

[18] Haubrich J, Gussone J, Barriobero-Vila P, Kürnsteiner P, Jägle EA, Raabe D, et al. The role of lattice defects, element partitioning and intrinsic heat effects on the microstructure in selective laser melted Ti-6Al-4V. Acta Materiala 2019;167:136–48. http://dx.doi.org/10.1016/j.actamat.2019.01.039.

[19] Thäsler T, Holtmannspötter J, Gudladth H-J. Monitoring the fatigue crack growth behavior of composite joints using in situ 2D-digital image correlation. J Adhes 2019;95(5–7):595–613. http://dx.doi.org/10.1080/00218464.2018.1562923.

[20] Dengg A, Kralovec C, Schagerl M. Damage monitoring of pinned hybrid composite–titanium joints using direct current electrical resistance measurement. Compos Struct 2024;334:117972. http://dx.doi.org/10.1016/j.compstruct.2024.117972.

[21] Habenicht G. Kleben: grundlagen, technologie, anwendungen. Vol. 457, Berlin Heidelberg: Springer-Verlag; 2009, http://dx.doi.org/10.1007/978-3-540-85266-7.

[22] Bagnato T, Ravindran AR, Mirabedini A, Ladani RB, Kandare E, Orifici AC, et al. Superior interfacial toughening of hybrid metal-composite structural joints using 3D printed pins. Composites A 2023;168:107479. http://dx.doi.org/10.1016/j.compositesa.2023.107479.

[23] Martin A, Hinkelmann K, Esderts A. Zur Auswertung von Schwingfestigkeitsversuchen im Zeitfestigkeitsbereich. Mater Test 2011;53(9):502–12. http://dx.doi.org/10.3139/120.110255.